One step synthesis of oxygen doped porous graphitic carbon nitride with remarkable improvement of photo-oxidation activity: Role of oxygen on visible light photocatalytic activity

Pengxiang Qiu [a], Chenmin Xu [a], Huan Chen [a,*], Fang Jiang [a,*], Xin Wang [b], Ruifeng Lu [c], Xirui Zhang [c]

[a] Key Laboratory of Jiangsu Province for Chemical Pollution Control and Resources Reuse, School of Environmental and Biological Engineering, Nanjing University of Science and Technology, Nanjing 210094, China
[b] Key Laboratory of Soft Chemistry and Functional Materials, Nanjing University of Science and Technology, Ministry of Education, Nanjing 210094, China
[c] Department of Applied Physics, Nanjing University of Science and Technology, Nanjing 210094, China

ARTICLE INFO

ABSTRACT

A novel metal-free oxygen doped porous graphitic carbon nitride (OA-g-C_3N_4) was synthesized by condensation of oxalic acid and urea. The 40% OA-g-C_3N_4 catalyst can degrade bisphenol A ($15\,mg\,L^{-1}$) in 240 min with a mineralization rate as high as 56%. The markedly higher visible-light-driven oxidation activity of OA-g-C_3N_4 is attributed to the porous morphology and unique electrical structure. The porous structure of OA-g-C_3N_4 provides more active sites for adsorption and degradation of pollutants. Moreover, oxygen atoms in the tri-s-triazine units help to extend sufficient light absorption range up to 700 nm, improve the separation of charge-carriers and alter the position of valence band (VB) and conduction band (CB). The VB edge shifts from 1.95 eV to 2.46 eV due to the incorporation of O atoms, which leads to the change of active species in the photocatalytic reaction. Trapping experiment shows that superoxide radicals play the major role in the photocatalytic degradation of BPA on g-C_3N_4, while hydroxyl radical is the dominant active species in the photocatalytic degradation process over 40% OA-g-C_3N_4. This study presents a simple, economical and environment-friendly method to synthesized oxygen doped porous graphitic carbon nitride.

© 2017 Elsevier B.V. All rights reserved.

1. Introduction

Water pollution has become a serious environmental problem in China with the rapid economic development and industrialization [1]. As an economical and environmentally friendly oxidation technology, photocatalysis has great potential in wastewater treatment [2]. The oxidation activity of photocatalyst is crucial for wastewater treatment, especially for organic compounds degradation. However, traditional photocatalysts, such as TiO_2, only response to ultraviolet light due to the wide band gap, and cannot take full advantage of the solar energy [3]. Thus, the research of novel visible-light-driven (VLD) photocatalyst with high oxidation activity has attracted much attention.

Graphitic carbon nitride (g-C_3N_4), a metal-free VLD photocatalyst with a narrow band gap of 2.7 eV, has become a hot research topic in photocatalysis. [4]. In addition, g-C_3N_4 is nontoxic, highly stable and can easily be synthesized via one-step polymerization of the cheap raw material. However, g-C_3N_4 suffers from several disadvantages, such as low specific surface area, limited visible light absorption capacity and high recombination rate of photoinduced charge carriers [5]. Currently, it has been reported that the more ideal the chemical structure g-C_3N_4 is, the weaker activity it behaves in some catalytic processes, for that the structure defects and surface terminations may play an important role on photocatalytic activity [6]. Non-metal (e.g., B, P, F, C and O [7–10]) doping is a conventional method to increase the structure defects of g-C_3N_4, in order to alter the position of conductive band (CB) and valence band (VB), improve the separation rate of charge carriers and create more active sites to elevate the catalytic activity. For example, C doped g-C_3N_4 showed extensive visible light absorption and enhanced electrical conductivity due to the change of intrinsic electronic and band structure. The photocatalytic activity of C

doped g-C$_3$N$_4$ in degradation of rhodamine B, reduction of Cr(VI) and hydrogen production was significantly improved [11]. Li et al. [12] synthesized oxygen-doped g-C$_3$N$_4$ by a hydrothermal method using H$_2$O$_2$, and the obtained catalyst performed enhanced photocatalytic activity under visible light irradiation. Recently, Huang et al. [13] reported a porous oxygen-doped g-C$_3$N$_4$ catalyst synthesized by condensation of melamine and H$_2$O$_2$, which exhibited 7.8 times higher H$_2$ evolution activity than pristine g-C$_3$N$_4$. Clearly, it is still highly desirable to explore the modification of g-C$_3$N$_4$ to achieve large light adsorption range and low charge recombination rate with enhanced oxidation activity.

Changing morphology is another approach to promote the catalytic performance, since larger surface area can provide more active sites for reaction and the textural structure may have influence on the electronic structure of photocatalyst. For instance, porous structure can promote the light adsorption due to multiple-reflection effect and suppress the recombination of photogenerated electron-hole pairs on account of the shortened diffusion distance [14,15]. Porous g-C$_3$N$_4$ catalysts have been synthesized through various methods, such as hard-template method [16], soft-template method [17], acid protection [18] and gas bubbling in the calcination process [19]. Nevertheless, it remains a challenge to simultaneously modify the pore-structure and achieve the non-metal doping of g-C$_3$N$_4$ through a facile and environment-friendly strategy.

Herein, we present a simple, economical and environment-friendly method to synthesize oxygen doped porous g-C$_3$N$_4$ (OA-g-C$_3$N$_4$) by condensation of oxalic acid and urea for the first time. The synthesized OA-g-C$_3$N$_4$ not only possesses high surface area but also extends the sufficient light absorption range up to 700 nm, which significantly enhances the degradation efficiency of bisphenol A (BPA) under visible light irradiation. The oxygen atoms incorporate into the network of g-C$_3$N$_4$ by replacing the sp^2 N atoms, which markedly influences the electrical structure of g-C$_3$N$_4$. The results show that 40% OA-g-C$_3$N$_4$ can degrade BPA with initial concentration of 15 mg L^{-1} in 240 min under visible light. Cycling tests showed that OA-g-C$_3$N$_4$ is still highly efficient after 5 rounds. Trapping experiments are conducted to explore the degradation mechanism. This research provides a brand new approach to achieve the oxygen doping in the polymeric g-C$_3$N$_4$ with superior photocatalytic activity.

2. Experimental section

2.1. Synthesis of photocatalyst

2.1.1. Synthesis of g-C$_3$N$_4$

The g-C$_3$N$_4$ was synthesized by the polymerization of urea [20]. 20 g of urea was placed in a porcelain crucible with a cover and calcined at 550 °C for 5 h with a heating rate of 3 °C min^{-1}.

2.1.2. Synthesis of OA-g-C$_3$N$_4$

The porous oxygen-doped graphitic carbon nitride samples were synthesized by condensation of oxalic acid and urea under high temperature for the first time. In detail, 20 g of urea was mixed with a certain amount of oxalic acid by grinding in a mortar. The resultant powders were placed in a porcelain crucible with a cover and calcined at 550 °C for 5 h with a heating rate of 3 °C min^{-1}. The obtained samples were designated as x OA-g-C$_3$N$_4$ (where x is the weight ratio of oxalic acid to urea, x = 10%, 20%, 30%, 40%, 50%, respectively). The condensation of dicyandiamide and oxalic acid was carried out in the same process.

2.1.3. Synthesis of mesoporous graphitic carbon nitride (mpg-C$_3$N$_4$)

20 g of urea was dissolved in 50 mL of solution at 60 °C. Then, 2 g of silica particles (Aladdin, China) with diameter of 15 nm was added into the solution and the mixture was stirred for 8 h at 60 °C. The resulting powder was calcined at 550 °C with a rate of 3 °C min^{-1} in the air. The product was stirred in 4 mol L^{-1} NH$_4$HF for 24 h to remove the silica template. At last, the obtained product was washed with distilled water and ethanol, and dried at 70 °C overnight.

2.2. Characterization

Transmission electron microscopy (TEM) image was observed on a JEOL JEM2100 microscopy at an acceleration voltage of 200 kV. The specific surface area was measured by N$_2$ adsorption-desorption on Micromeritics ASAP 2000. Before each measurement, the samples were out-gassed at 260 °C for 6 h under vacuum. Powder X-ray diffraction (XRD) patterns were acquired from a Bruker D8 Advanced diffraction-meter with Cu Kα radiation with a scanning angle ranging from 10° to 80°. The distribution of the elements (C, N and O) in the sample was analyzed using energy dispersive X-ray spectroscopy (EDX) equipped with the TEM (Titan G2 60–300). The content of C, N, O and H was measured by the elemental analyzer (CHN-O-Rapid, Heraeus). X-ray photoelectron spectrum (XPS) and valence band X-ray photoelectron spectra (VBXPS) were obtained on a PHI-5000C VersaProbe system (UlVAC-PHI) with Al Kα radiation. The Fourier transform infrared (FT-IR) experiment was acquired on a Nexus 870 spectrometer. ^{13}C cross-polarisation magic angle spinning nuclear magnetic resonance spectrum (^{13}C NMR) was recorded by a Bruker Avance 400 spectrometer at room temperature with a 4 mm triple resonance Bruker MAS probe spinning at 14 kHz. Electron paramagnetic resonance (EPR) spectrum was acquired using a JOEL JES-FA200 spectrometer. UV–vis diffuse reflectance spectrum (DRS) was taken on a Hitachi U-3010 UV–vis spectrometer. Dielectric constant was measured on an N5244A PNA-X microwave network analyzer. The Schottky curve was obtained on CHI 660E electrochemical workstation equipped with a standard three-electrode system (a platinum foil electrode as the counter electrode and an Ag/AgCl electrode as the reference electrode.). Time-resolved fluorescence decay spectrum was performed on an Edinburgh FLSP920 spectrophotometer with the excitation wavelength at 340 nm. Photoluminescence spectrum (PL) was measured on a jobinYvon SPEX Fluorolog-3-P spectroscope. Photocurrent transient response was carried out on a CHI 660 B electrochemical workstation in a standard three-electrode system under illumination using a 300 W Xe lamp.

2.3. Photocatalytic degradation of BPA

The photocatalytic activities of the samples were conducted by degradation of bisphenol A (BPA) under visible light irradiation. In a typical run, 0.02 g catalyst was added into 50 mL of 15 mg L^{-1} BPA solution in a quartz tube reactor at 25 °C. The mixture was kept stirring in dark for 60 min to reach adsorption-desorption equilibrium before a 500 W Xe lamp was turned on. At given time intervals of irradiation, 2 mL of suspension was withdrawn and then filtered. The concentration of BPA was determined by high performance liquid chromatography (e2685, Waters) equipped with a UV–vis detector (2489, Waters).

2.4. Adsorption of BPA

20 mg of photocatalyst was added into 50 mL of BPA solution with initial concentration of 15 mg L^{-1} and kept stirring at 25 °C
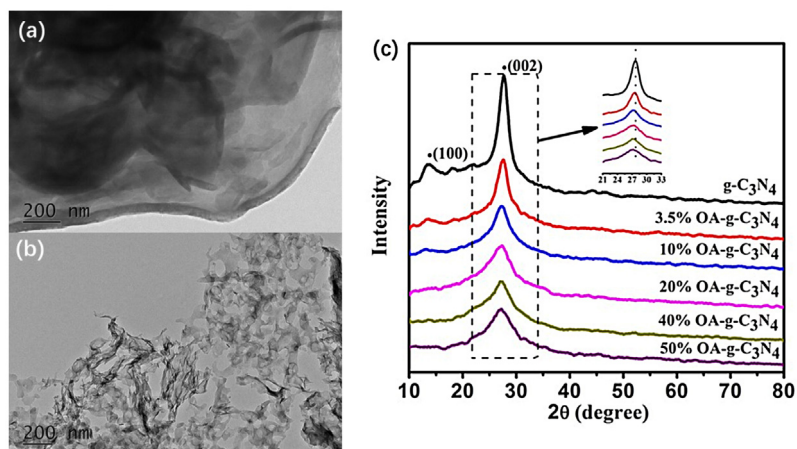
Fig. 1. The TEM images of (a) bulk g-C_3N_4 and (b) 40% OA-g-C_3N_4, and (c) the XRD patterns of bulk g-C_3N_4 and x OA-g-C_3N_4.

with a magnetic stirrer. The samples were taken periodically and filtrated with 0.45 μm membrane.

3. Results and discussion

3.1. Morphology and chemical structure of OA-g-C_3N_4

The morphology of g-C_3N_4 and x OA-g-C_3N_4 was investigated via transmission electron microscopy (TEM). As shown in Fig. 1a, the pristine g-C_3N_4 presents a thick and interlayer-like structure without obvious pores. Interestingly, the morphology changes tremendously in x OA-g-C_3N_4 (Fig. 1b). In detail, the TEM image of 3.5% OA-g-C_3N_4 (Fig. S1b) shows a porous structure and the other x OA-g-C_3N_4 catalysts are further thinned and fragmentized with the increased OA content (Fig. S1c–S1f). The pore structures of OA-g-C_3N_4 may be ascribed to two reasons: (a) OA may serve as the template in the polymerization and decompose into CO_2 during the calcination process [21] and (b) OA may react with part of the amino groups in the urea and affect their subsequence thermal condensation [19]. As seen in Table 1, the BET surface areas of x OA-g-C_3N_4 samples are gradually increased from 35.3 to 105.2 $m^2\,g^{-1}$ as the content of oxalic acid increased from 0 to 40%. However, the BET surface area of 50% OA-g-C_3N_4 (99.1 $m^2\,g^{-1}$) is lower than that of 40% OA-g-C_3N_4, probably due to the over-fragmentization of 50% OA-g-C_3N_4.

The change of morphology through oxygen-doping can also be confirmed by the results of X-ray diffraction (XRD). As shown in Fig. 1c, the XRD patterns of the pristine g-C_3N_4 shows two main

reflections at 2θ = 13.1° and 27.5°. The strong peak at 27.5° indexed as (002) is attributed to the interlayer stacking of aromatic systems. It is worth noting that the (002) peak displays a slight shift to lower angles in x OA-g-C_3N_4 samples, suggesting the increase of interlayer distance in x OA-g-C_3N_4 [22]. The weak characteristic peak at 13.1° is indexed as (100) and represents the in-plane structural packing motif [23]. The decrease of (100) p eak is ascribed to the decreased planar size of the layers [24], which is in good agreement with the results of TEM.

The distribution of the elements (C, N and O) in 40% OA-g-C_3N_4 was analyzed using energy dispersive X-ray spectroscopy equipped with the transmission electron microscopy (TEM-EDX). As shown in Fig. S2, the C, N, O elements are uniformly distributed on the surface of 40% OA-g-C_3N_4 in the scanned area. The content of each element in g-C_3N_4 and x OA-g-C_3N_4 was measured by elementary analysis. As the OA contents increase from 3.5% to 50% in x OA-g-C_3N_4 catalysts, the contents of C show a slight alteration, while the contents of N decrease from 61.1% to 52.8% and the contents of O increase from 2.0% to 8.9% (Table 1). Thus, a speculation that part of nitrogen in tri-s-triazine units was replaced by oxygen was raised, and the results of X-ray photoelectron spectroscopy (XPS), fourier transform infrared spectroscopy (FTIR), ^{13}C solid state nuclear magnetic resonance (NMR) and electron paramagnetic resonance (EPR) confirmed this speculation.

The XPS spectra were performed to investigate the elemental valence state and composition in g-C_3N_4 and 40% OA-g-C_3N_4, and the survey spectra are shown in Fig. S3. The main C 1s spectrum of the pristine g-C_3N_4 (Fig. 2a) can be fitted into three peaks at

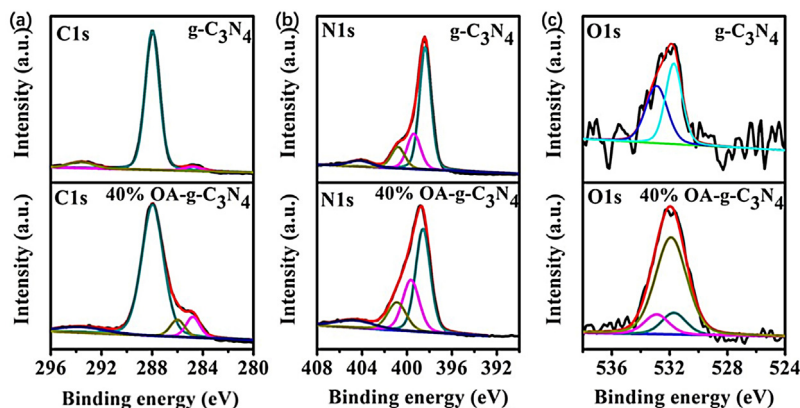**Fig. 2.** The high resolution (a) C 1s, (b) N 1s, (c) O 1s XPS spectra of g-C_3N_4 and 40% OA-g-C_3N_4.

Table 1
Elemental contents, BET surface areas, band gaps and initial rate of BPA degradation over g-C_3N_4 and x OA-g-C_3N_4.

Photocatalyst	Element content (wt%)				BET surface area ($m^2 g^{-1}$)	Pore volume ($cm^3 g^{-1}$)	Band gap (eV)	Initial rate[a] ($mmol\, g_{cat}^{-1} h^{-1}$)
	C	N	H	O				
g-C_3N_4	34.3	61.1	2.0	2.0	35.3	0.14	2.91	0.020
3.5% OA-g-C_3N_4	34.3	61.1	2.0	2.0	48.3	0.22	2.82	0.035
10% OA-g-C_3N_4	34.0	59.2	2.2	3.7	59.6	0.28	2.15	0.048
20% OA-g-C_3N_4	34.6	59.0	2.1	4.0	84.6	0.40	2.12	0.058
40% OA-g-C_3N_4	34.0	55.3	2.4	7.3	105.2	0.48	2.08	0.098
50% OA-g-C_3N_4	34.6	52.8	2.5	8.9	99.1	0.44	2.07	0.071

[a] In a typical run, 0.02 g catalyst was added into 50 mL of 15 mg L^{-1} BPA solution in a quartz tube reactor at 25 °C. The mixture was kept stirring in dark for 60 min to reach adsorption-desorption equilibrium before a 500 W Xe lamp was turned on.

293.6, 288.0 and 284.8 eV, respectively. The three peaks are corresponded to π excitation, sp^2-bonded carbon (N=C—N) and graphitic carbon, respectively [25]. Surprisingly, the C 1s spectrum of 40% OA-g-C_3N_4 exhibits a new peak at 286.0 eV compared with that of g-C_3N_4. This new peak could be attributed to the C atoms bonded with O (C—O) [26,27]. Table 1S shows that there is a remarkable decrease of N=C—N and increase of C—O in 40% OA-g-C_3N_4 compared with that of g-C_3N_4. It reflects that N is probably replaced by O in 40% OA-g-C_3N_4. In addition, the N 1s spectrum of pristine g-C_3N_4 (Fig. 2b) was divided into four peaks at 404.2, 400.8, 399.4 and 398.4 eV, which are corresponded to π-excitation, amino functional groups (C_2—N—H), tertiary N atoms(C_3—N), and C—N=C, respectively [20]. As shown in Table 2S, C—N=C content of 40% OA-g-C_3N_4 decreases as compared to that of g-C_3N_4. This result is consistent with the result of C 1s, confirming the decrease of sp^2 N in 40% OA-g-C_3N_4. Moreover, The O 1s spectrum of g-C_3N_4 (Fig. 2c) was fitted into two peaks at 532.9 and 531.7 eV, which are ascribed to the adsorbed water and C=O from CO_2 or incompletely polymerized precursor [28], respectively. A new peak at 531.9 eV appears in 40% OA-g-C_3N_4, attributing to C—O—C species [14,29].

The chemical structure of g-C_3N_4 and x OA-g-C_3N_4 was further studied through FTIR (Fig. 3a). The multiple bands at 1200–1600 cm^{-1} are ascribed to the characteristic CN heterocycle stretches, and the sharp band at 800 cm^{-1} corresponds to the breathing mode of the heptazine units [30]. The pristine g-C_3N_4 and x OA-g-C_3N_4 catalysts exhibit these characteristic bands, suggesting that the backbone structure of OA-g-C_3N_4 is almost as same as that of g-C_3N_4. It is noteworthy that the peak at 1238 cm^{-1} (attributed to stretching vibration of C—N bond) shifts to higher frequencies with increased OA amount, which indicates that part of C—N is transformed into C—O since the stretching vibration peak of C—O bond appears at higher frequencies due to the higher electronegativity of O atoms.

The ^{13}C solid state nuclear magnetic resonance was taken to investigate the chemical state of C. As shown in Fig. 3b, two peaks, centered at 164.8 and 156.8 ppm, can be observed from the spectrum of g-C_3N_4, which are attributed to CN_2—NH_x and CN_3, respectively [31]. The intensity of peak at 156.8 ppm decreases in the spectrum of 40% OA-g-C_3N_4, probably due to the fragmentization of g-C_3N_4. Besides, the peaks in spectrum of 40% OA-g-C_3N_4 show shoulders at 160.5 and 151.6 ppm, suggesting the appearance of new state C atoms caused by incorporation of O atoms. The shoulders at high field may result from the increasing electron density of C atoms owing to the introduction of lone pair electrons of O atoms.

In attempt to obtain more evidence relative to the structure alternation due to the O doping, EPR was conducted to detect the spin state of unpaired electrons (Fig. 3c). The bulk g-C_3N_4 exhibits one single Lorentzian line with a *g* factor of 2.003 due to the unpaired electron of the π-bonded aromatic rings [32]. The EPR intensity of 40% OA-g-C_3N_4 is greatly enhanced, which can be ascribed to the increasing of defect sites owing to the enlargement of surface area [33]. Moreover, a shoulder peak appears at

325.95 mT, probably because substituting the N atom in the heptazine unit with an O atom creates one unpaired spin. On the basis of the characterization results, the possible chemical structure of OA-g-C_3N_4 is proposed in Fig. 3d. A part of the sp^2 N atoms in the heptazine units were replaced by O atoms in x OA-g-C_3N_4 during the calcination process. The condensation of dicyandiamide and oxalic acid was also carried out for comparison (Fig. S4a). Similarly, the weight ratio of oxalic acid to dicyandiamide was 0.4, and the obtained product was named as 40% OA-g-C_3N_4/D. The photocatalytic performance of 40% OA-g-C_3N_4/D is slightly better than g-C_3N_4 synthesized using dicyandiamide (g-C_3N_4/D) in the photocatalytic degradation of BPA (Fig. S4b), indicating that the electron structure has no significant change in 40% OA-g-C_3N_4/D. As shown in Fig. S4c, 40% OA-g-C_3N_4/D exhibits little difference compared with g-C_3N_4/D in the UV–vis diffuse reflectance spectra, indicating that the chemical structure is almost unvaried when the oxalic acid is added in the synthesis process. Thus, it can be inferred that oxygen atoms from oxalic acid was prone to incorporated into heptazine units only when urea is used as precursors. It was reported that urea turned into isocyanic acid, biuret, cyanuric acid and melamine step by step [20], while dicyandiamide could turn into melamine directly before g-C_3N_4 was generated [34]. All of the processes of urea reaction to melamine are beneficial to oxygen doping into melamine, and then the oxygen-containing melamine consequently polymerize to oxygen-doped g-C_3N_4.

3.2. The photochemical properties of OA-g-C_3N_4

The photochemical properties of g-C_3N_4 and x OA-g-C_3N_4 were explored by UV–vis diffuse reflectance spectrum (DRS), photocurrent transient responses, time-resolved photoluminescence (PL) spectrum, PL spectrum and Mott-Schottky curve. The UV–vis DRS of g-C_3N_4 and x OA-g-C_3N_4 are shown in Fig. 4a. The adsorption edge of x OA-g-C_3N_4 shows a remarkable red-shift (480–700 nm) compared to that of g-C_3N_4 (460 nm). The corresponding band gaps of these samples decrease from 2.91 and 2.07 eV as calculated from the Kubelka-Munk method (Fig. S5). The change of the color of x OA-g-C_3N_4 is another proof for oxygen-doping (Fig. S6), since x OA-g-C_3N_4 presents much deeper color than g-C_3N_4. The oxygen-doping can lead to the red-shift of adsorption edge, and porous structure of OA-g-C_3N_4 with multiple-reflection effect of incident light can be responsible for the overall improvement of light adsorption intensity [35]. The photocurrent transient responses (Fig. 4b) were measured under simulated sunlight and darkness at 0.0 V vs SCE in 0.5 M Na_2SO_4 aqueous solution. The photocurrent of 40% OA-g-C_3N_4 electrode is much higher than that of bulk g-C_3N_4 electrode, suggesting the enhanced photoelectrical property of 40% OA-g-C_3N_4. The increase of photocurrent may be ascribed to two aspects: one is the increased light absorption intensity and the extensive light absorption range promoted the effective visible light harvest of 40% OA-g-C_3N_4; the other is the separation
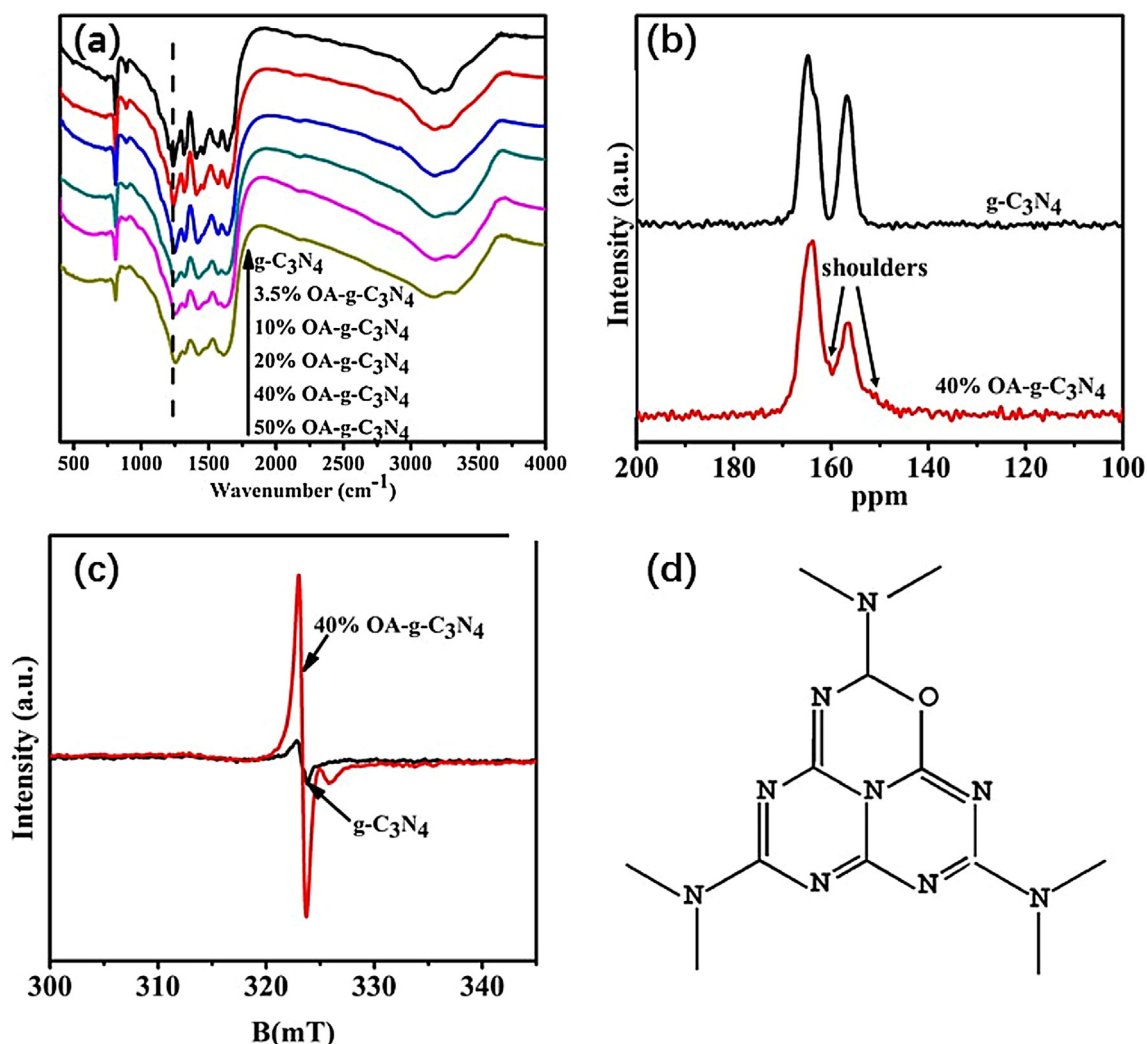
Fig. 3. (a) the FTIR spectra of g-C$_3$N$_4$ and x OA-g-C$_3$N$_4$, (b) the NMR spectra of g-C$_3$N$_4$ and 40% OA-g-C$_3$N$_4$, (c) the EPR spectra of g-C$_3$N$_4$ and 40% OA-g-C$_3$N$_4$ diagram of tri-s-triazine unit and (d) diagram of O-doped tri-s-triazine unit.

efficiency of photogenerated electron-hole pairs was improved by oxygen-doping and porous structure.

Time-resolved PL experiments were performed to determine the charge carrier lifetime of g-C$_3$N$_4$ and x OA-g-C$_3$N$_4$. As shown in Fig. 4c, the life time of charge carriers decreases with the increase of OA content, from 3.719 ns for pristine g-C$_3$N$_4$ to 0.820 ns for 50% OA-g-C$_3$N$_4$. The shortened life time of charge carriers may be resulted from the efficient charge separation due to the porous structure and oxygen doping [36]. Shorter life time of charge carriers was reported to be related to higher turnover frequency (TOF) of photocatalytic H$_2$ generation [37]. The PL spectra of g-C$_3$N$_4$ and x OA-g-C$_3$N$_4$ are presented in Fig. 4d. The emission peak attributed to the radiative recombination of photogenerated electron-hole pairs is used to evaluate the transfer and separation efficiency of photogenerated charge carriers. Thus, the lower emission peak of x OA-g-C$_3$N$_4$ suggests the recombination of charge carriers is highly suppressed due to the enhanced migration of electron-hole pairs. This may be resulted from the possible contributions from at least three aspects as follows: (1) the lone electron pairs of incorporated oxygen atom are delocalized to the oxygen-doped aromatic system, which increased the charge density and mobility [17]; (2) an internal electric field in favor of the electron-hole separation is formed due to the lattice strain from the change of C—N bond length and electronic polarisation effect [13]; (3) the diffusion path of photo-

generated electron-hole pairs from internal to surface of catalyst is highly shortened due to the porous structure.

The flat band potential (E$_{fb}$) and carrier density (N$_D$) can be calculated from Mott-Schottky curve (Fig. S7) [38]. The E$_{fb}$ is estimated from the intercept value on the x-axis by extrapolating Mott-Schottky plot, and the N$_D$ is estimated from the slope of Mott-Schottky curve according to Eqs. (1) and (2) [39]:

$$\frac{1}{C^2} = \frac{2}{e\varepsilon\varepsilon_o N_D}\left(E - E_{fb} - \frac{\kappa T}{e}\right) \tag{1}$$

$$N_D = \frac{2}{e\varepsilon\varepsilon_0}\left[\frac{d\left(\frac{1}{C^2}\right)}{d(E)}\right]^{-1} \tag{2}$$

where C is the capacitance of the space charge layer; E is the potential versus normal hydrogen electrode (NHE), and in this case, E = E (Ag/AgCl) + 0.197 eV; e is the electron charge (1.602 × 10^{-19}C); ε is the dielectric constant; ε_0 is the vacuum permittivity (8.85 × 10^{-14} F cm^{-1}) and κ is the Boltzmann constant (1.38 × 10^{-23} J K^{-1}). The ε of g-C$_3$N$_4$ is measured to be 15.6. The N$_D$ of 40% OA-g-C$_3$N$_4$ are estimated to be 2.25 × 10^{20} cm^{-3}, which is 3.75 times higher than that of g-C$_3$N$_4$ (4.73 × 10^{19} cm^{-3}). The results of carrier density show that charge transport efficiency is
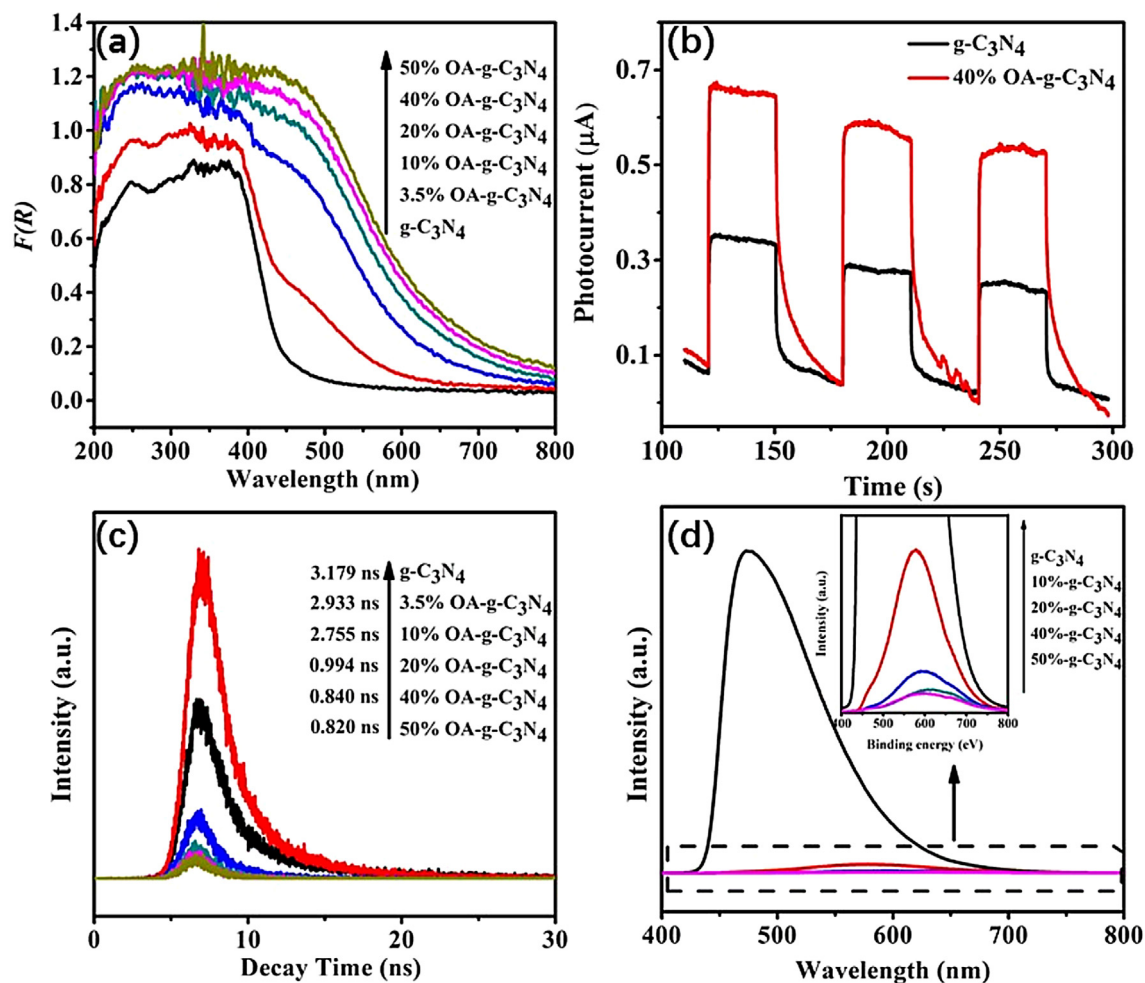
Fig. 4. (a) UV–vis diffuse reflectance spectra of g-C$_3$N$_4$ and x OA-g-C$_3$N$_4$, (b) photocurrent transient responses of g-C$_3$N$_4$ and 40% OA-g-C$_3$N$_4$, (c) time-resolved PL and (d) PL spectra of g-C$_3$N$_4$ and x OA-g-C$_3$N$_4$.

enhanced with oxygen doping [39], which is consistent with the experimental result of PL.

3.3. Photocatalytic activity enhancement

3.3.1. Photodegradation and adsorption of bisphenol A (BPA)

Photodegradation of bisphenol A (BPA) under visible light was used to evaluate the photocatalytic performance of g-C$_3$N$_4$ and x OA-g-C$_3$N$_4$ catalysts. As shown in Fig. 5a, only 30% of BPA is degraded by pristine g-C$_3$N$_4$ after 240 min, while the BPA is completely decomposed by 40% OA-g-C$_3$N$_4$ within 180 min. The initial rate of BPA degradation on bulk g-C$_3$N$_4$ and x OA-g-C$_3$N$_4$ is presented in Table 1. The as-prepared OA-g-C$_3$N$_4$ shows a high initial degradation rate (0.098 mmol g$_{cat}^{-1}$ h^{-1}) of bisphenol A (BPA) under visible light, which is 4.7 times higher than that of bulk g-C$_3$N$_4$. The mineralization rates of BPA by g-C$_3$N$_4$ and 40% OA-g-C$_3$N$_4$ catalysts are also estimated through total organic carbon (TOC). As shown in Fig. S8, the photocatalytic mineralization rates of BPA over g-C$_3$N$_4$ and 40% OA-g-C$_3$N$_4$ under 240 min' visible light irradiation are 3% and 56%, respectively. The adsorption of BPA on g-C$_3$N$_4$ and OA-g-C$_3$N$_4$ is also investigated. As shown in Fig. S9 no significant adsorption of BPA on g-C$_3$N$_4$ or OA-g-C$_3$N$_4$ can be observed.

3.3.2. Stability of photocatalyst

To evaluate the stability of the as-prepared photocatalyst, a five-cycle recycling experiment was performed over 40% OA-g-C$_3$N$_4$. In the first round, 50 mL of 15 mg L^{-1} BPA solution was mixed with 0.02 g photocatalyst in a quartz tube reactor. Before irradiation with a 500 W Xe lamp, the mixture was kept stirring in dark for 60 min. The final sample was obtained at 180 min and then centrifuged to collect the photocatalyst in the sample. The photocatalyst in the remaining BPA solution was also collected by centrifugation. The collected photocatalyst was then washed with distilled water and dried at 65 °C over night for the next round. As shown in Fig. 5b, the photocatalytic activity decreases from 100% to 93% after five rounds of cycling. This may be ascribed to the loss of photocatalyst particles during the recycling runs and/or experimental error. This result demonstrates the high stability of 40% OA-g-C$_3$N$_4$ and suggests its potential for application in environmental remediation.

3.3.3. Mechanism of photodegradation

The mechanism of photocatalysis was investigated by species trapping experiments to determine the main active species generated during the photocatalytic process. Scavengers of t-butyl alcohol (t-BuOH), KI and 4-hydroxy-2,2,6,6-tetramethylpiperidine-N-oxyl (TEMPOL) were added to trap •OH, h$^+$ and O$_2$•$^-$, respectively [40]. As shown in Fig. 6a, the removal rate of BPA on bulk g-C$_3$N$_4$ is reduced to 1.5% in the presence of TEMPOL, while only a weak inhibition can be observed on the degradation of BPA with addition of
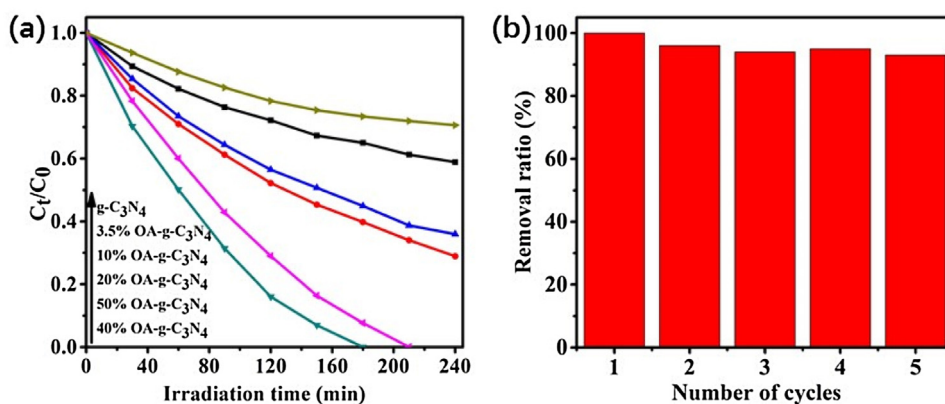
Fig. 5. (a) BPA degradation experiments of g-C_3N_4 and x OA-g-C_3N_4 and (b) cycling runs for the degradation over 40% OA-g-C_3N_4. Reaction condition: 0.4 g L^{-1} photocatalyst, 15 mg L^{-1} BPA, 25 °C. The irradiation time of every cycle is 180 min.
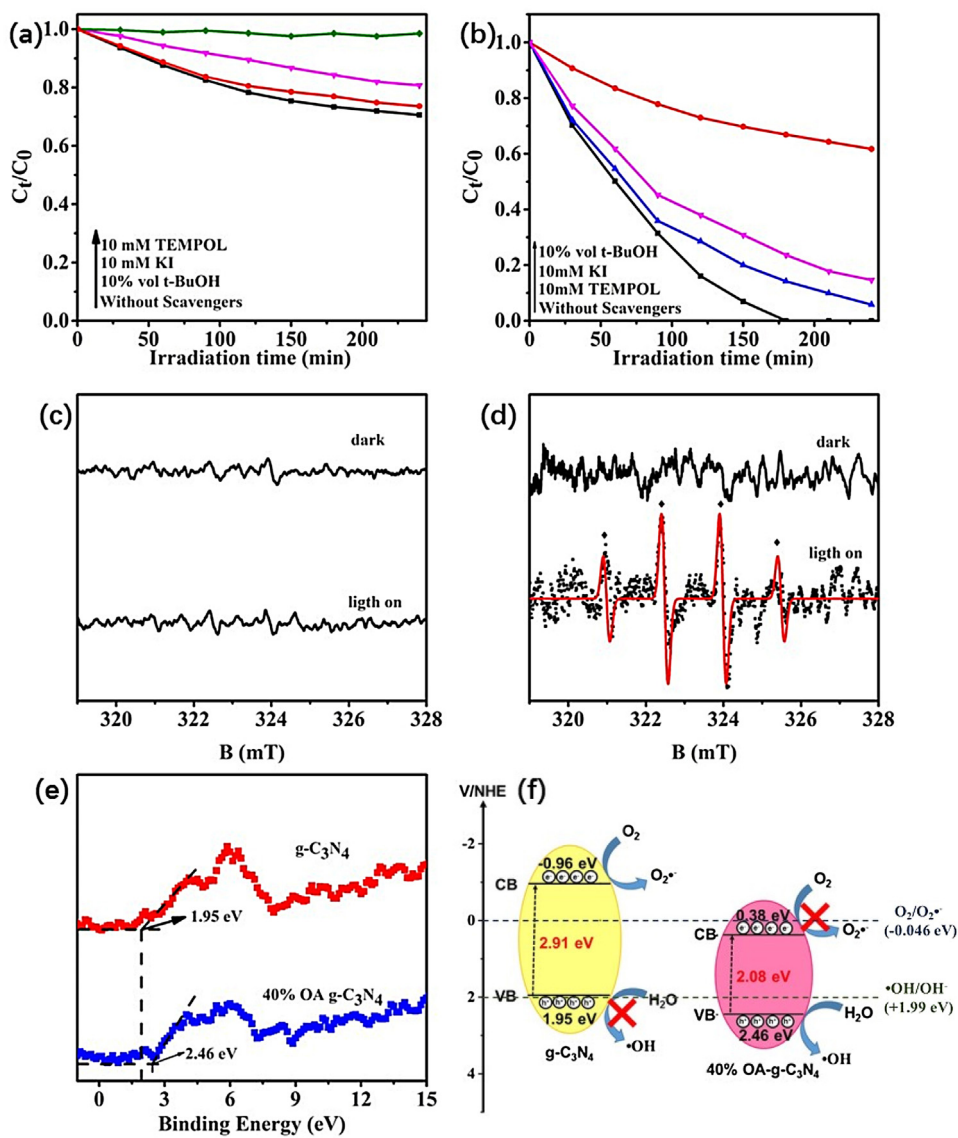

Fig. 6. The effect of TEMPOL, KI and t-BuOH on the degradation of BPA on (a) g-C_3N_4 and (b) 40% OA-g-C_3N_4. The EPR spectrum of DMPO/•OH in the presence of (c) g-C_3N_4 and (d) 40% OA-g-C3N4. (e) The VBXPS of g-C_3N_4 and 40% OA-g-C_3N_4 and (f) the proposed mechanism for photocatalytic process.

t-BuOH and KI, indicating that $O_2 \bullet^-$ should be the dominant active species in this photodegradation process and h$^+$ as well as $\bullet$OH plays a minor role to the photocatalytic reaction. For comparison, the trapping experiments of active species during the photocatalytic reaction of 40% OA-g-C$_3$N$_4$ were tested (Fig. 6b). It can be found that photocatalytic efficiency decreases dramatically with the addition of t-BuOH. However, no significant decrease in the removal rate of BPA in the presence of KI and TEMPOL is observed. This indicates that $\bullet$OH plays a dominant role in the photocatalytic degradation by 40% OA-g-C$_3$N$_4$. The formation of $\bullet$OH by 40% OA-g-C$_3$N$_4$ is further confirmed by an EPR trap technique with 5,5-dimethyl-1-pyrroline-*N*-oxide (DMPO). DMPO serves as a radical scavenger of stable DMPO/$\bullet$OH species. Obviously, the incorporation of oxygen atoms changes the photocatalytic mechanism. As shown in Fig. 6d, four peaks with the relative intensities of 1:2:2:1 clearly appears with the addition of 40% OA-g-C$_3$N$_4$ in the EPR spectrum under the visible light irradiation, which is considered to be the characteristic spectrum for the DMPO/$\bullet$OH adduct [41]. No obvious EPR signal is observed in the dark time. Furthermore, no DMPO/$\bullet$OH signal (Fig. 6c) can be found with the addition of bulk g-C$_3$N$_4$ neither in the darkness nor under visible light irradiation. This is consistent with the result that $\bullet$OH is dominant active species in the 40% OA-g-C$_3$N$_4$ photocatalytic system, while $\bullet$OH plays a minor role in the g-C$_3$N$_4$ system.

The valence band (VB) position of photocatalyst was measured by valence band X-ray photoelectron spectroscopy (VBXPS). As shown in Fig. 6e, the valence band edge of 40% OA-g-C$_3$N$_4$ downshifts to 2.46 eV compared with that of g-C$_3$N$_4$ (1.95 eV), which may result from the incorporation of O atoms into tri-s-triazine units. Combining the results of UV–vis DRS and VBXPS, the schematic band structure of g-C$_3$N$_4$ and 40% OA-g-C$_3$N$_4$ is presented in Fig. 6f. The CB potential of g-C$_3$N$_4$ (-0.96 eV vs NHE) is more negative than E^0 ($O_2/O_2\bullet^-$ = −0.046 eV vs NHE), and the VB potential of g-C$_3$N$_4$ (1.95 eV vs NHE) is not more positive than E^0 ($\bullet$OH/OH$^-$ = +1.99 eV vs NHE) [42]. Therefore, the electrons on the surface of g-C$_3$N$_4$ could react with O_2 to form $O_2\bullet^-$, while the holes could not oxidize OH$^-$/H$_2$O to generate $\bullet$OH directly in bulk g-C$_3$N$_4$ photocatalytic system. In contrast, The VB potential of 40% OA-g-C$_3$N$_4$ (2.46 eV vs NHE) is more positive than E^0 ($\bullet$OH/OH$^-$ = +1.99 eV vs NHE), and the CB potential of 40% OA-g-C$_3$N$_4$ (0.38 eV vs NHE) is not more negative than E^0 ($O_2/O_2\bullet^-$ = −0.046 eV vs NHE). This indicates that $\bullet$OH could be directly formed in the photocatalytic process and $O_2\bullet^-$ could not. The $\bullet$OH radicals play a major role on many photocatalytic systems, such as the degradation of BPA [43], phenol [44], dyes [45] and bacterial inactivation [46] according to the literature. Thus, it is reasonable to suppose that 40% OA-g-C$_3$N$_4$ has great potential in the degradation of organic pollutants through $\bullet$OH formed under visible light irradiation.

In general, the superior photocataytic activity of OA-g-C$_3$N$_4$ is attributed to the unique electrical structure and porous morphology. The incorporation of O atoms into the tri-s-triazine units extends sufficient light absorption range up to 700 nm, suppresses the recombination of charge carriers, and alters the position of VB and CB. The VB edge shifted from 1.95 eV to 2.46 eV, which attributes to the change of active species in the photocatalytic reaction. Secondly, the porous structure could adsorb more light because of high specific surface area and multiple-reflection effect. Besides, the enlargement of specific surface area leads to the increase of the number of active sites, which causes the improvement of BPA adsorption and degradation. Thus, the changes of both the chemical structure and morphology have the synergistic effect on the elevation of photocatalytic activity of OA-g-C$_3$N$_4$. Notably, the degradation efficiency of BPA slightly decreases when the initial percentage of OA is as high as 50%. The excess of oxygen in 50% OA-g-C$_3$N$_4$ leads to excessive defects, which may act as the recombination centers and suppress the photocatalytic activity. Besides,

the smaller surface area of 50% OA-g-C$_3$N$_4$ may be responsible for the decrease in photocatalytic efficiency. In order to investigate the main factor to the improvement of efficiency, mesoporous graphitic carbon nitride (mpg-C$_3$N$_4$) with specific surface area of 142.5 m^2 g^{-1} was synthesized. The photocatalytic degradation of BPA on mpg-C$_3$N$_4$ is presented in Fig. S10. The initial rate of BPA degradation on mpg-C$_3$N$_4$ is 0.049 mmol gcat^{-1} h^{-1}, which indicates that both of the enlargement of surface area and the O doping are the main factors for the enhanced photocatalytic activity.

4. Conclusion

A new method by changing precursor was developed to prepare an oxygen-doped porous g-C$_3$N$_4$ (x OA-g-C$_3$N$_4$) photocatalyst. The 40% OA-g-C$_3$N$_4$ photocatalyst exhibited high specific surface area (105.2 m^2 g^{-1}), promoted the separation efficiency of photogenerated electron-hole pairs, and extended light adsorption edge (up to 700 nm) owing to the oxygen-doped heptazine units and porous structure. The as-prepared oxygen-doped porous g-C$_3$N$_4$ could decompose BPA within 180 min with a high initial rate of 0.098 mmol g$_{cat}^{-1}$ h^{-1}, which is 4.7 times higher than that of bulk g-C$_3$N$_4$. The incorporation of oxygen atoms led to the defects in g-C$_3$N$_4$ structure and increased the charge density and mobility, which significantly improved the photocatalytic activity. The valence band position of 40% OA-g-C$_3$N$_4$ (2.46 eV) is more positive than E^0 ($\bullet$OH/OH$^-$ = +1.99 eV vs NHE), and trapping experiment shows that hydroxyl radicals play the major role in the photocatalytic degradation of BPA over 40% OA-g-C$_3$N$_4$. This research demonstrates an easy and green method to prepare oxygen-doped porous g-C$_3$N$_4$, which provides a useful approach to design and fabricate high efficient photocatalyst for pollutant removal.

Appendix A. Supplementary data

Supplementary data associated with this article can be found, in the online version, at http://dx.doi.org/10.1016/j.apcatb.2017.01.058.

References

[1] Q. Wang, Z. Yang, Environ. Pollut. 218 (2016) 358–365.
[2] N. Liang, J. Zai, M. Xu, Q. Zhu, X. Wei, X. Qian, J. Mater. Chem. A 2 (2014) 4208–4216.
[3] Y. Yang, J. Wen, J. Wei, R. Xiong, J. Shi, C. Pan, ACS Appl. Mater. Int. 5 (2013) 6201–6207.
[4] Y. Wang, X. Wang, M. Antonietti, Angew. Chem. Int. Ed. 51 (2012) 68–89.
[5] Z. Zhao, Y. Sun, F. Dong, Nanoscale 7 (2015) 15–37.
[6] Y. Wang, J. Zhang, X. Wang, M. Antonietti, H. Li, Angew. Chem. Int. Ed. 49 (2010) 3356–3359.
[7] Y. Wang, H. Li, J. Yao, X. Wang, M. Antonietti, Chem. Sci. 2 (2011) 446–450.
[8] Y. Wang, Y. Di, M. Antonietti, H. Li, X. Chen, X. Wang, Chem. Mater. 22 (2010) 5119–5121.
[9] G. Liu, P. Niu, C. Sun, S.C. Smith, Z. Chen, G.Q. Lu, H.M. Cheng, J. Am. Chem. Soc. 132 (2010) 11642–11648.
[10] Y. Zhang, T. Mori, J. Ye, M. Antonietti, J. Am. Chem. Soc. 132 (2010) 6294–6295.

[11] G. Dong, K. Zhao, L. Zhang, Chem. Comm. 48 (2012) 6178–6180.
[12] J. Li, B. Shen, Z. Hong, B. Lin, B. Gao, Y. Chen, Chem. Commun. 48 (2012) 12017–12019.
[13] Z.F. Huang, J. Song, L. Pan, Z. Wang, X. Zhang, J.J. Zou, W. Mi, X. Zhang, L. Wang, Nano Energy 12 (2015) 646–656.
[14] S. Li, J. Chen, F. Zheng, Y. Li, F. Huang, Nanoscale 5 (2013) 12150–12155.
[15] D.W. Wang, F. Li, M. Liu, G.Q. Lu, H.M. Cheng, Angew. Chem. 120 (2008) 379–382.
[16] X. Wang, K. Maeda, X. Chen, K. Takanabe, K. Domen, Y. Hou, X. Fu, M. Antonietti, J. Am. Chem. Soc. 131 (2009) 1680–1681.
[17] J. Ran, T.Y. Ma, G. Gao, X.W. Du, S.Z. Qiao, Energy Environ. Sci. 8 (2015) 3708–3717.
[18] G. Dong, W. Ho, Y. Li, L. Zhang, Appl. Catal. B: Environ. 174 (2015) 477–485.
[19] F. He, G. Chen, Y. Yu, Y. Zhou, Y. Zheng, S. Hao, Chem. Commun. 51 (2015) 425–427.
[20] Y. Zhang, J. Liu, G. Wu, W. Chen, Nanoscale 4 (2012) 5300–5303.
[21] M. Wu, J.M. Yan, X.W. Zhang, M. Zhao, Appl. Surf. Sci. 354 (2015) 196–200.
[22] W. Ho, Z. Zhang, W. Lin, S. Huang, X. Zhang, X. Wang, Y. Huang, ACS Appl. Mater. Int. 7 (2015) 5497–5505.
[23] C. Chang, Y. Fu, M. Hu, C. Wang, G. Shan, L. Zhu, Appl. Catal. B: Environ. 142 (2013) 553–560.
[24] P. Niu, L. Zhang, G. Liu, H.M. Cheng, Adv. Funct. Mater. 22 (2012) 4763–4770.
[25] P. Qiu, H. Chen, F. Jiang, RSC Adv. 4 (2014) 39969–39977.
[26] J. Oh, R.J. Yoo, S.Y. Kim, Y.J. Lee, D.W. Kim, S. Park, Chem. Eur. J. 21 (2015) 6241–6246.
[27] Y. Fu, J. Zhu, C. Hu, X. Wu, X. Wang, Nanoscale 6 (2014) 12555–12564.
[28] J. Liu, T. Zhang, Z. Wang, G. Dawson, W. Chen, J. Mater. Chem. 21 (2011) 14398–14401.
[29] L.N. Bùi, M. Thompson, N.B. McKeown, A.D. Romaschin, P.G. Kalman, Analyst 118 (1993) 463–474.
[30] D. Dontsova, S. Pronkin, M. Wehle, Z. Chen, C. Fettkenhauer, G. Clavel, M. Antonietti, Chem. Mater. 27 (2015) 5170–5179.
[31] Y. Cui, Z. Ding, X. Fu, X. Wang, Angew. Chem. Int. Ed. 51 (2012) 11814–11818.
[32] J. Fang, H. Fan, M. Li, C. Long, J. Mater. Chem. A 3 (2015) 13819–13826.
[33] G. Zhang, J. Zhang, M. Zhang, X. Wang, J. Mater. Chem. 22 (2012) 8083–8091.
[34] J. Liu, T. Zhang, Z. Wang, G. Dawson, W. Chen, J. Mater. Chem. 21 (2011) 14398–14401.
[35] T. Zhao, Z. Liu, K. Nakata, S. Nishimoto, T. Murakami, Y. Zhao, L. Jiang, A. Fujishima, J. Mater. Chem. 20 (2010) 5095–5099.
[36] J. Chen, S. Shen, P. Guo, P. Wu, L. Guo, J. Mater. Chem. A 2 (2014) 4605–4612.
[37] M. Shalom, M. Guttentag, C. Fettkenhauer, S. Inal, D. Neher, A. Llobet, M. Antonietti, Chem. Mater. 26 (2014) 5812–5818.
[38] Z. Hu, G. Liu, X. Chen, Z. Shen, J.C. Yu, Adv. Funct. Mater. 26 (2016) 4445–4455.
[39] Y. Liu, L. Liang, C. Xiao, X. Hua, Z. Li, B. Pan, Y. Xie, Adv. Energy Mater. (2016) 1600437.
[40] P. Qiu, J. Yao, H. Chen, F. Jiang, X. Xie, J. Hazard. Mater. 317 (2016) 158–168.
[41] L. Gu, J. Wang, Z. Zou, X. Han, J. Hazard. Mater. 268 (2014) 216–223.
[42] L. Ye, J. Liu, Z. Jiang, T. Peng, L. Zan, Appl. Catal. B: Environ. 142 (2013) 1–7.
[43] A.O. Kondrakov, A.N. Ignatev, F.H. Frimmel, S. Bräse, H. Horn, A.I. Revelsky, Appl. Catal. B: Environ. 160 (2014) 106–114.
[44] M. Diak, M. Klein, T. Klimczuk, W. Lisowski, H. Remita, A. Zaleska-Medynska, E. Grabowska, Appl. Catal. B: Environ. 200 (2017) 56–71.
[45] J.T. Spadaro, L. Isabelle, V. Renganathan, Environ. Sci. Technol. 28 (1994) 1389–1393.
[46] L.S. Zhang, K.H. Wong, H.Y. Yip, C. Hu, J.C. Yu, C.Y. Chan, P.K. Wong, Environ. Sci. Technol. 44 (2010) 1392–1398.